

Brushy C-Decorated BiTe-Based Thermoelectric Film for Efficient Photodetection and Photoimaging

Rongke Sun, Runan Guo, Xue Yu, Yanmei Ren, Ruoxi Wang, Pinggen Zou, Zhi Chen, Rui Xu, Yanqing Ma,* and Lei Ma*



Cite This: <https://doi.org/10.1021/acsami.4c07979>



Read Online

ACCESS |



Metrics & More



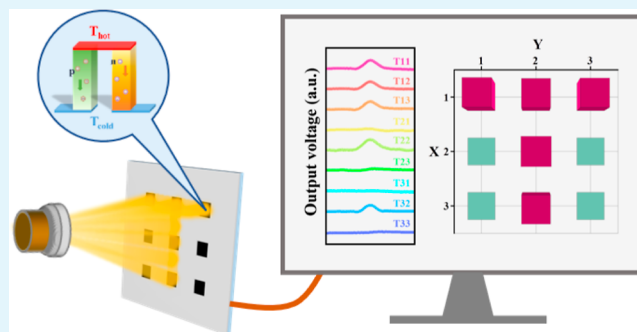
Article Recommendations



Supporting Information

ABSTRACT: Current strategies for simultaneously achieving high thermoelectric performance and high light absorption efficiency still suffer from complex steps and high costs. Herein, two kinds of amorphous thermoelectric films of n-type Bi_2Te_3 and p-type $\text{Bi}_{0.5}\text{Sb}_{1.5}\text{Te}_3$ with high Seebeck coefficients were prepared by pulsed laser deposition (PLD) technology. In addition, C-decorated films with excellent light absorption efficiency at the junction of the thermoelectric legs were prepared by simple drop coating and reactive ion etching (RIE) method. The TE/C-RIE composite device exhibits excellent photodetection performance under the conditions of simulated natural light, monochromatic light, and high-frequency chopping. The maximum responsivity and specific detectivity of the device can reach 153.58 mV W^{-1} and $6.97 \times 10^6 \text{ cm Hz}^{1/2} \text{ W}^{-1}$ (under simulated natural light), respectively. This represents an improvement rate of 85.91% compared to that of the pure TE device. Benefiting from the excellent photodetection efficiency of the device and integration advantage of PLD technology, the composite structure can be expanded into integrated photoimaging devices. The accurate identification of patterned light sources with letters (T, J, and U) and digitals (0–9) was successfully realized by associating the response electrical signals of each electrode with the position coordinates. This work provides valuable guidance for the design and fabrication of wide-spectrum photodetectors and complex optical imaging devices.

KEYWORDS: photothermoelectric effect, BiTe-based thermoelectric film, brush-like C layer, photodetection, photoimaging



1. INTRODUCTION

With the development of electronic technology, photodetectors have gained significant attention in sensing,¹ communication,² environmental monitoring,³ imaging,⁴ and biological detection^{5,6} fields. Nowadays, the mainstream photodetectors are typically composed of narrow band gap semiconductor heterojunctions or field-effect transistors prepared by two-dimensional materials. Such type of photodetectors generally operate with essential external refrigeration and auxiliary bias.⁷ Meanwhile, the detection wavelength range is limited by the band gap of optoelectronic semiconductors.⁸ Therefore, it is of great significance to develop a wide-spectrum response photodetector that can operate independently at room temperature. Photothermoelectric (PTE) detectors represent a new detection mode based on the photothermal effect and thermoelectric effect. It is expected to achieve fast wide-spectrum photodetection without external bias at room temperature.⁹

Light responsivity is a crucial parameter for evaluating the performance of PTE photodetectors⁷ as it is directly related to the Seebeck coefficient of the thermoelectric material and the photogenic temperature difference. Increasing the Seebeck coefficient of thermoelectric materials can lead to a larger

voltage output at a small temperature difference.^{10,11} Currently, researchers primarily focus on preparing low-dimensional Te-based nanowire films with high Seebeck coefficient through dimension reduction treatments^{8,12,13} and further assemble high-performance PTE photodetectors by cutting and splicing the nanowire films.^{14,15} However, the need for electrode connections between the thermoelectric legs such as copper wire or silver glue hinders the realization of a multifunctional integrated preparation. Physical deposition technologies such as magnetron sputtering,¹⁶ evaporation coating,¹⁷ and PLD¹⁸ can be combined with micro–nano-processing technology to prepare highly integrated thermoelectric thin films with specific patterns.^{17,19} Among these techniques, the pulsed laser deposition (PLD) technology exhibits excellent component retention characteristics. The crystallinity of the deposited films can be precisely controlled by varying the type of

Received: May 15, 2024

Revised: July 15, 2024

Accepted: July 29, 2024

substrate,^{20,21} which is well-suited for the preparation of high Seebeck coefficient thermoelectric films. BiTe-based thermoelectric materials have a rhombohedral crystal structure of the space group $R\bar{3}m$, due to which they are considered as one of the best thermoelectric materials ($ZT > 1$) that work near room temperature.^{22–24} In the BiTe materials family, the typical n-type Bi_2Te_3 and p-type $\text{Bi}_{0.5}\text{Sb}_{1.5}\text{Te}_3$ are easy to be processed into commercial targets and used in the field of physical deposition because of their relatively simple composition. At the same time, the intrinsically small band gap structure (theoretical calculated value: Bi_2Te_3 : 0.15 eV²⁵ and $\text{Bi}_{0.5}\text{Sb}_{1.5}\text{Te}_3$: 0.2 eV²⁶) makes the material have a wide application potential in the field of PTE devices.

Due to the higher surface smoothness of physically deposited films, the light absorption efficiency is low. Therefore, current research efforts aim to enhance the light absorption efficiency of composite devices by modifying the auxiliary light absorption unit on the surface of thermoelectric thin films. One approach involves decorating noble metal particles on the surface of thermoelectric materials to enhance the interaction between light and matter through the plasmon resonance effect, which results in the temperature increase of the photosensitive region.^{27–29} However, the optical wavelength induced by the plasmon resonance effect is strictly dependent on the particle size of noble metal particles.^{30,31} It seriously complicates the fabrication of devices. In addition, some researchers have tried to modify the light absorption layer with a special structure on the surface of thermoelectric thin films by electrochemical synthesis and other technologies. For instance, the electrodeposition of a weedy-like polypyrrole structure can improve the light absorption efficiency of composite devices by enhancing the reflection times of incident light on the surface complex structure.³² However, the reaction potential supplied in the electrochemical deposition process can easily cause irreversible damage to the bottom thermoelectric electrodes. Therefore, it is crucial to explore a simple and nondestructive method to improve the light absorption efficiency of thermoelectric composite devices.

In this work, PLD technology was used to prepare BiTe-based thermoelectric films with ultrahigh Seebeck coefficient (Bi_2Te_3 : $-188.6 \mu\text{V K}^{-1}$ and $\text{Bi}_{0.5}\text{Sb}_{1.5}\text{Te}_3$: $500.6 \mu\text{V K}^{-1}$). Then the brush-like C layer at the junction of thermoelectric legs was modified by utilizing a combination of simple drop coating and reactive ion etching (RIE) methods. The light absorption efficiency of the composite can be increased to more than 95% in the range of 400–900 nm by virtue of the special rough structure. The TE/C-RIE composite device achieves excellent light detection performance under different illumination conditions. Which the responsivity is 85.91% higher than that of TE device. The expanded integrated photoimaging device successfully realized the accurate identification of pattern-shaped light sources by associating the electrical signals with the corresponding position coordinates. This work offers valuable insights and guidance for the development of wide-spectrum detection and complex optical imaging devices.

2. EXPERIMENTAL SECTION

2.1. Materials. The materials used were glass (Cat. no. 7105, Yancheng Feizhou Glass Co., Ltd.), n- Bi_2Te_3 and p- $\text{Bi}_{0.5}\text{Sb}_{1.5}\text{Te}_3$ targets [99.9%, Yipin Chuancheng (Beijing) Technology Co., Ltd.], Cu target (99.99%, Hefei Kejing Material Technology Co., Ltd.), silicone sealant (Kafuter, K-704N, Guangdong Hengda New Material

Technology Co., Ltd.), graphite spray [PR03094, CRC Industries Trading (Shanghai) Co., Ltd.], and polydimethylsiloxane and curing agent [PDMS, SYLGARD 184, Dow (America) Chemical Company]. All these materials were used as received without further processing unless otherwise specified.

2.2. Preparation of TE Films. Figure S1a shows the preparation process of the composite photodetector. First, the glass substrate (10 mm \times 10 mm \times 1 mm) was ultrasonically cleaned in acetone, ethanol, and deionized water, each for 10 min, and then dried in an oven for the deposition of the n-type Bi_2Te_3 and p-type $\text{Bi}_{0.5}\text{Sb}_{1.5}\text{Te}_3$ thermoelectric films. The deposition equipment shown in Figure S2 is a homemade direct writing pulse laser deposition system, in which the laser source (Quantel, Q-smart 450) wavelength and frequency were 532 nm and 20 Hz. The laser power and the beam spot were 35 mJ and 500 μm , respectively. During the deposition process, the distance between the target and the substrate was 10 mm, the included angle was about 10°, and the deposition pressure was 0.01 mbar. The two types thermoelectric films were deposited at room temperature for 40 min, respectively, and the deposition rate was about 2 nm min^{-1} . The deposited thermoelectric films were further annealed in a tubular furnace. Before annealing, the pressure in the furnace was stabilized to 0.04 mbar by N_2 (flow rate: 150 sccm) adjustment. The annealing temperatures were 100, 200, and 300 °C, and the annealing time was 2 h with a heating rate of 5 °C min^{-1} . Magnetron sputtering (VTC-16-D) was used to deposit Cu electrodes with a thickness of 50 nm at the junction of n- and p-type thermoelectric legs. The deposition current and pressure were 60 mA and 4 Pa, respectively. BiTe-based thermoelectric devices were obtained after deposition for 120 s, which were named TE.

2.3. Preparation of TE/C-RIE Devices for Photodetection. The TE device was further encapsulated with organic silicone sealant, and only the Cu connection electrode was exposed, for which the exposed area was 1 mm \times 1 mm. The encapsulated devices were dried on a hot plate at 50 °C for 30 min to make the sealant completely solidified. The graphite spray solution was drip-coated on the surface of the exposed Cu electrode with a dose of 0.6 $\mu\text{L mm}^{-2}$ to ensure the formation of a uniform carbon film with an equal thickness of 500 nm. The composite was placed on the hot plate at 50 °C for 20 min to completely cure the C film, and then the TE device modified with the C light absorption layer was obtained, which was named TE/C. The TE/C device was then placed in a reactive ion etching (RIE, SHL-100 μ) equipment with an O_2 (100 sccm) atmosphere for rough etching of the C film, where the etching power and time were 100 W and 30–360 s, respectively. The obtained TE/C device modified with the brush-like C layer after the etching process was named TE/C-RIE. In order to prepare the TE/C-RIE device for underwater testing, PDMS and curing agent were mixed at a ratio of 10:1 and then were coated on the surface of the C layer by drops after vacuum defoaming. The composite device was placed on the hot plate at 50 °C for 1 h for PDMS curing.

2.4. Preparation of TE/C-RIE Devices for Photoimaging. The substrate of photoimaging device was glass with the size of 10 mm \times 10 mm \times 1 mm, and the functional thermoelectric film was n-type Bi_2Te_3 , which has a better conductivity. The patterned matrix electrodes were made by adding a stainless-steel mask between the target and substrate during deposition, where the size of a single thermoelectric leg was 0.8 mm \times 2.5 mm and the responsive pixel size was 0.6 mm \times 0.6 mm. The preparation parameters of thermoelectric thin film, Cu electrode, and C light absorption layer and the packaging parameters of the device were the same as those of the photodetector, which will not be described here.

2.5. Characterizations. The surface morphology of samples was characterized by scanning electron microscopy (SEM, Hitachi, SU-3500) and atomic force microscopy (AFM, Park, NX10). Energy-dispersive X-ray spectroscopy (EDS, IXRF SYSTEM, SU-3500) was used to characterize the elemental components and distribution of materials. X-ray diffraction (XRD, TD3500, Cu $K\alpha$, $\lambda = 0.154 \text{ nm}$) and X-ray photoelectron spectroscopy (XPS, PerkinElmer, PHI 5100) were used to analyze the crystal structures and their chemical composition. The light absorption and reflection efficiencies of the

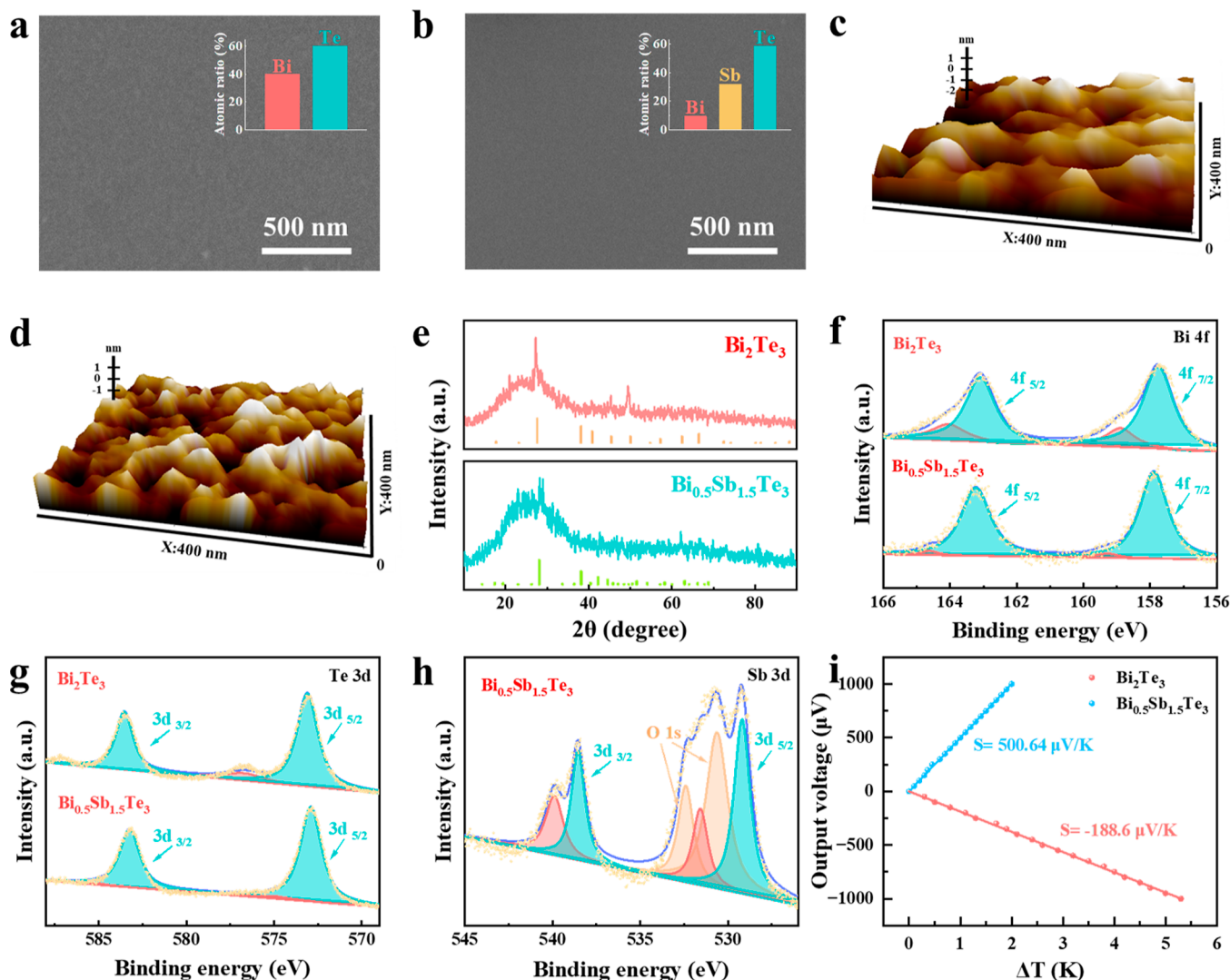


Figure 1. Characterizations of BiTe-based thermoelectric films prepared by PLD. (a,b) SEM images of n-type Bi_2Te_3 and p-type $\text{Bi}_{0.5}\text{Sb}_{1.5}\text{Te}_3$ films; the inset illustrations are the element ratio of Bi, Te and Bi, Sb, Te measured by EDS. (c,d) Surface morphologies of Bi_2Te_3 and $\text{Bi}_{0.5}\text{Sb}_{1.5}\text{Te}_3$ films characterized by AFM (contact mode). (e) XRD patterns of Bi_2Te_3 and $\text{Bi}_{0.5}\text{Sb}_{1.5}\text{Te}_3$ films. High-resolution XPS spectra of Bi 4f (f), Te 3d (g), and Sb 3d (h) of Bi_2Te_3 and $\text{Bi}_{0.5}\text{Sb}_{1.5}\text{Te}_3$. (i) Room-temperature Seebeck coefficients of Bi_2Te_3 and $\text{Bi}_{0.5}\text{Sb}_{1.5}\text{Te}_3$ annealed at 100°C .

devices were characterized by a UV-vis spectrophotometer (Hitachi, U-3900). The Seebeck coefficients of the thermoelectric films were characterized by a self-built test system, in which the heat source was the PI heating film, and the potential signal and temperature signal were, respectively, collected by a digital multimeter (Keysight, 34461A) and a digital thermocouple (K, UNI-T, UT320A). The conductivity of the materials was characterized by a four-probe tester (C-4, EVERBEING) and a digital source meter (Keithley, 2612B). A xenon lamp (LAR-X150, 220–1800 nm) and monochromator (WDG30, 330–900 \pm 0.2 nm) were used as light sources for photodetection and photoimaging tests of TE/C-RIE devices. The response electrical signals were collected by a digital multimeter (Keysight, 34461A). The intensity of the light source and photo-thermal conversion temperature of the composite device were characterized by a light intensity meter (CEL-NP2000) and a digital thermocouple (K, UNI-T, UT320A), respectively.

3. RESULTS AND DISCUSSION

The morphology of BiTe-based thermoelectric thin films deposited by PLD was characterized by SEM, as shown in Figure 1a,b. It can be observed that both types of films have smooth surfaces. AFM was used to perform contact-mode

surface scans of the films, as shown in Figure 1c,d. The Bi_2Te_3 film consists of particles with an average diameter of approximately 20 nm with a small surface roughness of about 2 nm, while the $\text{Bi}_{0.5}\text{Sb}_{1.5}\text{Te}_3$ film consists of particles with an average diameter of approximately 5 nm, with a surface roughness of about 1 nm, which is smoother than the Bi_2Te_3 film. EDS was utilized to characterize the elemental composition of the two films, and the atomic ratios of the elements are shown in the insets of Figure 1a,b. The raw data of the EDS characterization are presented in the inset tables of Figures S3 and S4. It can be observed that the Bi_2Te_3 film maintains a Bi/Te ratio of approximately 2:3, while the $\text{Bi}_{0.5}\text{Sb}_{1.5}\text{Te}_3$ film maintains a Bi/Sb/Te ratio of approximately 0.5:1.5:3. These ratios are consistent with the stoichiometric ratios of the targets, demonstrating the advantage of PLD technology in maintaining the chemical stoichiometry of the films.³³ The EDS mapping results in Figures S3 and S4 show the uniform distribution of the different elemental components within the Bi_2Te_3 and $\text{Bi}_{0.5}\text{Sb}_{1.5}\text{Te}_3$ films, which further confirm the ability of PLD to produce thermoelectric films with stable chemical stoichiometry and homogeneous composition. XRD

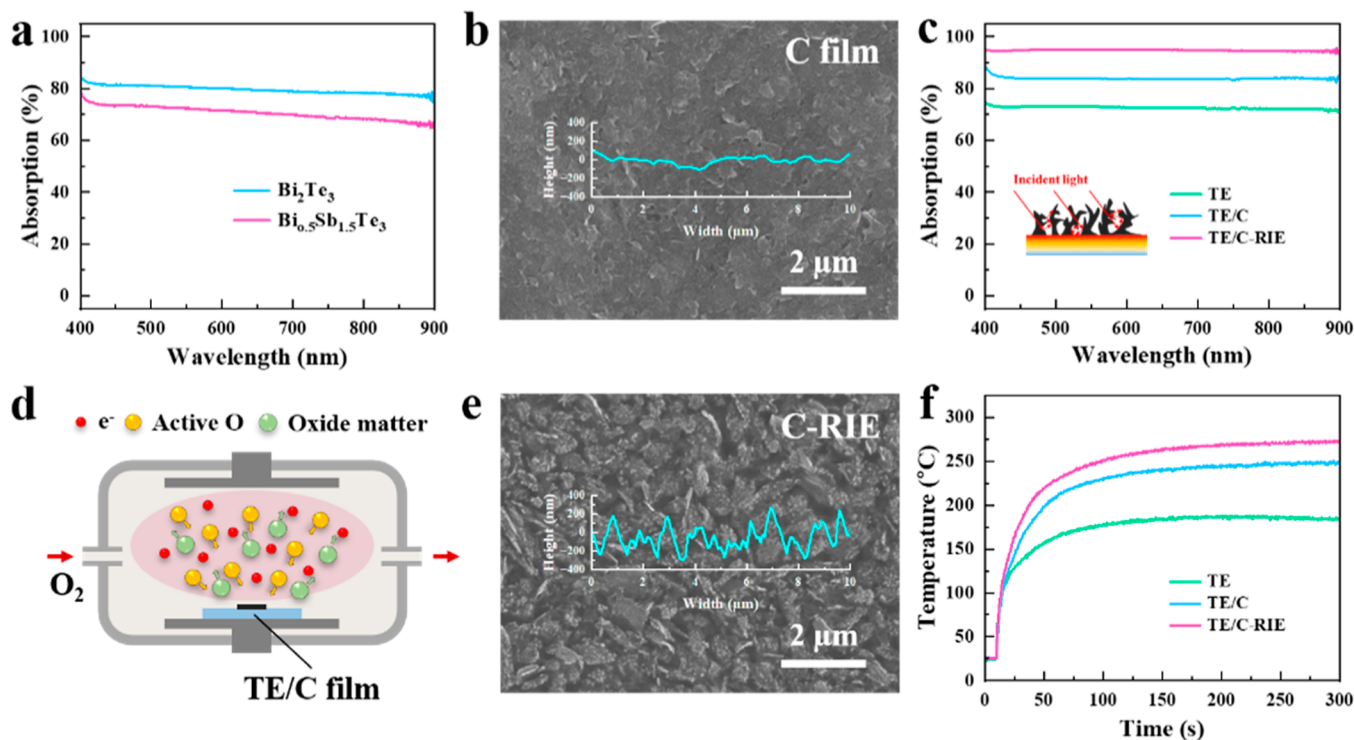


Figure 2. Light absorption efficiency, morphology, and photothermal conversion performance of different materials and devices. (a) Light absorption efficiency spectra of Bi₂Te₃ and Bi_{0.5}Sb_{1.5}Te₃ in the wavelength range of 400–900 nm. (b) SEM image of the C film; the inner illustration is the corresponding AFM morphological characterization. (c) Light absorption efficiency spectra of TE, TE/C, and TE/C-RIE in the wavelength range of 400–900 nm. (d) Schematic diagram of the mechanism of the RIE etching C film process. (e) SEM image of the C-RIE film; the inner illustration is the corresponding AFM morphological characterization. (f) Photothermal conversion test results of TE, TE/C, and TE/C-RIE under the light irradiation of 10 sun.

was employed to characterize the crystal structures of the two films, and the results are shown in Figure 1e. The XRD pattern of the Bi₂Te₃ film exhibits two weak diffraction peaks at 27.59 and 49.99°, corresponding to the (015) and (205) crystal planes of the hexagonal system (PDF#08-0027).^{20,34} However, no obvious diffraction peaks were observed in the results of Bi_{0.5}Sb_{1.5}Te₃ (PDF#49-1713), while the peaks in the range of 20–40° are derived from an amorphous glass substrate, as shown in Figure S5. The above results demonstrate that both films exhibit an amorphous state. Combined with the AFM characterization results, both the thermoelectric films are composed of particles with very small sizes. It leads to a low crystallization degree and significant grain boundary dispersion of these films. As a result, no significant X-ray diffraction peaks were observed in the XRD patterns. Further characterization and analysis of these two films were conducted using XPS techniques, and the results are shown in Figures S6 and 1f–h. In Figure S6a, the XPS spectrum of the Bi₂Te₃ film reveals clear peaks corresponding to elements C, O, Bi, and Te. A similar observation can be made in Figure S6b for the Bi_{0.5}Sb_{1.5}Te₃ film, which exhibits peaks corresponding to C, O, Bi, Sb, and Te. Figure 1f displays the fine XPS spectrum of the Bi 4f region for both films, where the peaks located at 163.09 and 157.81 eV correspond to the 4f_{5/2} and 4f_{7/2} spectra of the nonmetallic phase of Bi 4f, respectively.³⁵ A slight shift of approximately 0.1 eV can be observed in the Bi 4f peaks of the Bi_{0.5}Sb_{1.5}Te₃ film compared to that of the Bi₂Te₃ film. The peaks of 164.06 and 158.89 eV at higher binding energy are due to slight oxidation on the surface of the thermoelectric films.³⁶ Similarly, Figure 1g presents the fine XPS spectrum of

the Te 3d region for both films, where the peaks at 583.53, 573.10, 583.23, and 572.91 eV correspond to the 3d_{3/2} and 3d_{5/2} spectra of Te in the nonmetallic phase of Bi₂Te₃ and Bi_{0.5}Sb_{1.5}Te₃, respectively. The slight shifts of the Bi 4f and Te 3d peaks in the Bi_{0.5}Sb_{1.5}Te₃ film compared to that observed in the Bi₂Te₃ film are mainly attributed to the doping effect of the Sb element.³⁷ Figure 1h displays the fine spectrum of Sb 3d, where the peak at 538.56 eV corresponds to Sb 3d_{3/2}. The Sb 3d_{5/2} peak overlaps with the O 1s peak and is therefore typically not used for Sb element analysis.^{38,39} These results demonstrate the successful preparation of stoichiometrically stable and compositionally homogeneous thermoelectric thin films using the PLD technique.

In the experiments, annealing treatments at different temperatures were performed on the deposited thermoelectric films to optimize the electrical and thermoelectric properties. As shown in Figure S7a,b, with an increasing annealing temperature, the conductivities of Bi₂Te₃ and Bi_{0.5}Sb_{1.5}Te₃ gradually increased and reached optimal values at 300 °C, which were 771.8 and 236.1 S m⁻¹, respectively. This exhibits a significant improvement of 276 and 672% compared to those of the as-deposited samples. However, further increasing the annealing temperature resulted in the evaporation of the films due to their low boiling points. Figure S8 shows the XRD patterns of the two thermoelectric films as a function of the annealing temperature. It indicates that the degree of crystallization increased with enhancing annealing temperature. Therefore, the increased conductivity of Bi₂Te₃ and Bi_{0.5}Sb_{1.5}Te₃ can be attributed to improved crystallization of the materials. In contrast, as shown in Figure S7c,d, the room-

temperature Seebeck coefficients of Bi_2Te_3 and $\text{Bi}_{0.5}\text{Sb}_{1.5}\text{Te}_3$ decreased gradually with increasing annealing temperature. This is consistent with the inverse relationship between the Seebeck coefficient and conductivity with the change of carrier concentration.^{40–42} The Seebeck coefficients of Bi_2Te_3 and $\text{Bi}_{0.5}\text{Sb}_{1.5}\text{Te}_3$ thermoelectric films prepared at room temperature reached -212.6 and $522.5 \mu\text{V K}^{-1}$, respectively, which are higher values than those reported for similar BiTe-based thermoelectric films.^{43,44} After annealing at 100°C , the Seebeck coefficients of Bi_2Te_3 and $\text{Bi}_{0.5}\text{Sb}_{1.5}\text{Te}_3$ at room temperature were -188.6 and $500.6 \mu\text{V K}^{-1}$ (Figure 1i), showing a decrease of only 11 and 4% compared to that of the as-deposited samples. On the other hand, the conductivity, as shown in Figure S6a,b, increased by 147 and 190%, enabling stable output of the response signal while maintaining the maximum signal output magnitude. When the annealing temperature exceeded 100°C , the decrease in the Seebeck coefficient of $\text{Bi}_{0.5}\text{Sb}_{1.5}\text{Te}_3$ became more significant. Therefore, the Bi_2Te_3 and $\text{Bi}_{0.5}\text{Sb}_{1.5}\text{Te}_3$ films annealed at 100°C were used for the fabrication of the subsequent composite devices. At the same time, the negative Seebeck coefficient of Bi_2Te_3 indicates its n-type semiconductor characteristics, while $\text{Bi}_{0.5}\text{Sb}_{1.5}\text{Te}_3$ exhibits p-type semiconductor characteristics.

It is known that both Bi_2Te_3 and $\text{Bi}_{0.5}\text{Sb}_{1.5}\text{Te}_3$ are narrow band gap semiconductor materials with excellent light absorption capabilities,⁴⁴ as indicated in Figure 1a,b. These thermoelectric thin films exhibit high surface smoothness, which endows them with highly reflective characteristics like that of metals.⁴⁵ The light absorption efficiency of the films within the range of 400–900 nm was characterized using a UV–vis spectrophotometer, as shown in Figure 2a. It can be observed that the light absorption efficiencies of both Bi_2Te_3 and $\text{Bi}_{0.5}\text{Sb}_{1.5}\text{Te}_3$ are below 80% within the testing range. The light absorption efficiency of $\text{Bi}_{0.5}\text{Sb}_{1.5}\text{Te}_3$ further decreases to less than 70% after 700 nm. The high reflectivity of the films hinders the effective establishment of a temperature difference across the thermoelectric thin films.⁴⁶ Therefore, we enhance the light absorption efficiency of the thermoelectric films and improve the temperature of the photosensitive area of the composite device. A C absorption layer capable of absorbing half of the solar energy was applied via drop-casting at the junction position of Bi_2Te_3 and $\text{Bi}_{0.5}\text{Sb}_{1.5}\text{Te}_3$ electrodes.^{47,48} Figure 2b displays the surface morphology of the drop-casted C film, which consists of graphite flakes with an average size of approximately 300 nm. The surface roughness of the film, as observed through the AFM scan (Figure 2b inset), is approximately 100 nm. The light absorption efficiency of the devices with modified C films was then tested, as shown in Figure 2c. The pure TE device exhibited a light absorption efficiency of approximately 72% within the testing range. In comparison, the composite devices with modified C films showed a stable increase in light absorption efficiency to above 85% within the testing range, which is higher than that of the pure BiTe-based thermoelectric films. Inspired by the process of roughening the surface of PI film through RIE etching,⁴⁹ a similar approach was employed in the experiment to modify the surface of the C film on thermoelectric devices, which further increased the light absorption efficiency of the TE/C-RIE composite device to over 95%. The etching mechanism is illustrated in Figure 2d, where O_2 was used as the reactive gas in the RIE process. By ionizing O_2 under high voltage and reacting it with the C film, the edges of the graphite flakes within the original C film became the main reaction sites

during etching due to their larger structural defects. The nonuniform reaction rates within the film led to the roughening of the surface during the etching process. The influence of the RIE etching time on the surface morphology of the C film was investigated in the experiment, as shown in Figure S9a–f. Compared to the original C film, the edges of the graphite flakes gradually became recessed and exhibited island-like distribution after RIE etching. With increasing etching time, as shown in the SEM cross-sectional image in Figure S10b, the C film surface was gradually etched into a brush-like structure, and the surface roughness, as indicated in Table S1, showed a positive correlation with etching time. The light absorption efficiency of different etched samples in the range of 400–900 nm is shown in Figure S11. With an increasing etching time, the light absorption efficiency of the composite device gradually improved, reaching the highest performance after etching for 240 s. The light absorption efficiency of the composite device could consistently remain above 95% within the testing range. However, when the etching time exceeded 240 s, the light absorption efficiency of the composite device dropped to approximately 80%. As shown in Figure S9g,h, excessive etching time caused the C film to fall off from the surface of the device. It made the substrate exposed, resulting in a decrease in the light absorption efficiency of the composite device. Therefore, the drop-coated C film could achieve optimal light absorption enhancement after etching for 240 s by RIE. As shown in Figure 2e, the surface fluctuation height of the C absorption layer was approximately 500 nm, significantly higher than that of the original C film. To investigate the mechanism behind the enhancement in light absorption efficiency of C films through RIE treatment, a model was established, as shown in Figure S12a, to correlate the surface roughness of the films with their corresponding light absorption efficiency. A detailed description is provided in the Supporting Information. According to the simulation results, the changes in the surface structure of the material resulted in different reflection and scattering effects of the incident light on the material surface. When the surface roughness increased, the light absorption efficiency of the material improved by increasing the number of interactions between the incident light and the surface microstructure of the material. However, the relationship between the surface roughness of the film and its corresponding light absorption efficiency did not follow a linear trend. When the surface roughness of the material reached a higher degree, the light reflection and absorption of the material started to exhibit a restrictive effect, which led to a decrease in the light absorption efficiency. This conclusion provides guidance for improving the light absorption efficiency by roughening the surface of the thin films. To characterize the practical photothermal conversion ability of the devices, the surface temperatures of different composite devices were measured under 10 sun illumination. From Figure 2f, it can be observed that the surface temperature of the TE device rapidly increased to 92.2°C within 10 s and stabilized at 179.1°C after 100 s. In contrast, the stabilized temperatures of the TE/C and TE/C-RIE devices increased to 233.2 and 254.4°C , which represent an improvement rate of 42%. Therefore, it can be proven that the RIE etching process effectively enhances the photothermal conversion ability of the composite devices. This excellent photothermal conversion ability is attributed to the significantly increased surface roughness of the C film, which

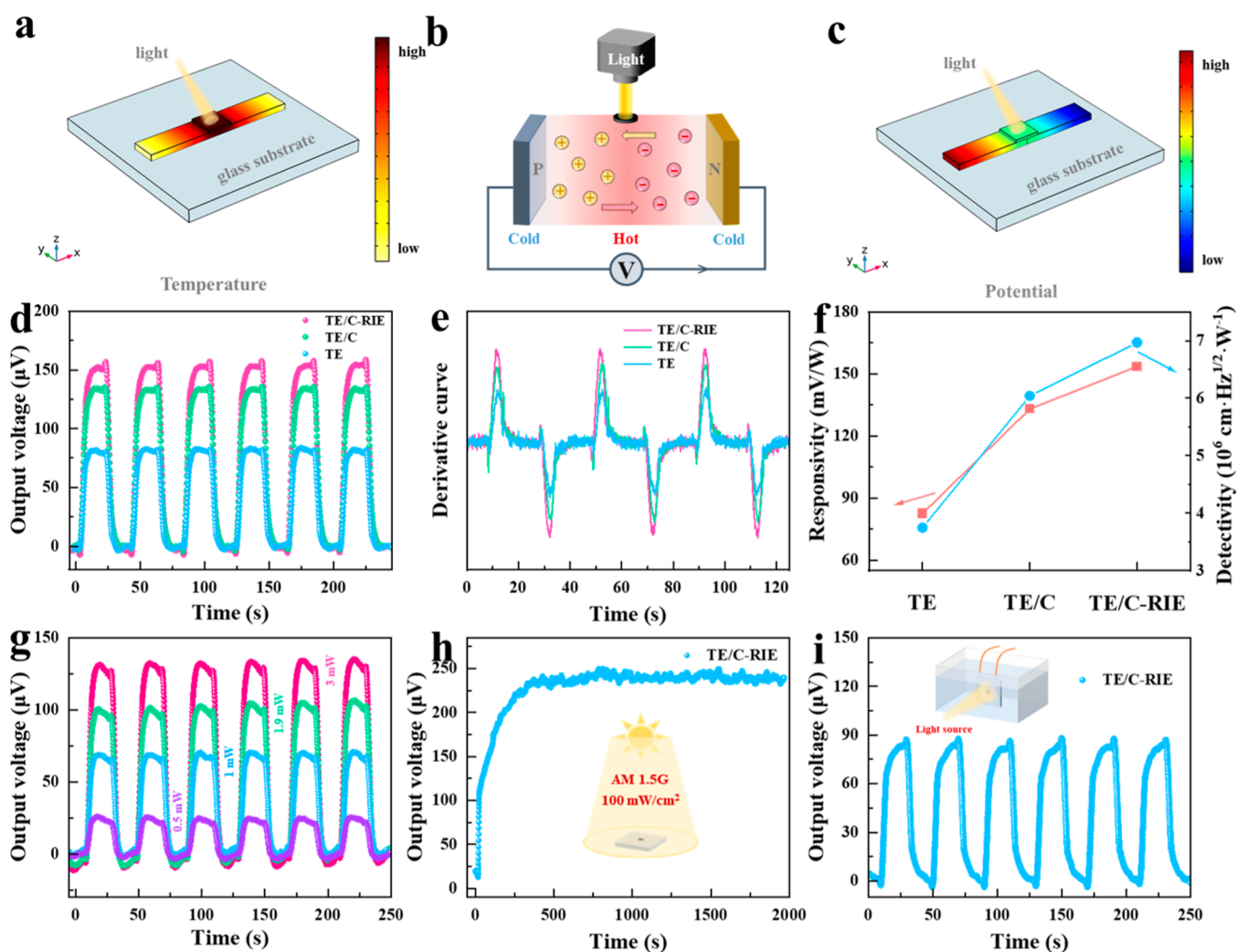


Figure 3. Light response performance of various devices under different natural light irradiation conditions. (a) Temperature field distribution of TE/C-RIE under light irradiation simulated by COMSOL. (b) Schematic diagrams of the PTE effect. (c) Potential field distribution of TE/C-RIE under light irradiation simulated by COMSOL. (d) Light response curves of TE, TE/C, and TE/C-RIE under 1 mW simulated natural light irradiation. (e) Differential transformation of light response curves of TE, TE/C, and TE/C-RIE. (f) Light responsivity and detectivity of TE, TE/C, and TE/C-RIE. (g) Light response curves of TE/C-RIE under light irradiation with different intensities. (h) Light response performance of TE/C-RIE fully exposed to 1 sun irradiation. (i) Underwater light response performance of TE/C-RIE under the irradiation of 1 sun.

effectively enhances the multiple absorption of incident light on the photosensitive region of the device.

The mechanism of the PTE effect of the TE/C-RIE device was elucidated by utilizing the COMSOL Thermoelectric Module. Figure 3a displays the temperature distribution of the device. It shows that the C-RIE photosensitive region effectively raises the temperature of the thermoelectric leg junction through the photothermal effect of the C layer, while the outer sides of the thermoelectric legs remain at room temperature. Each thermoelectric leg exhibits a temperature gradient that gradually increases from the outer to the inner side. On this basis, as shown in the working mechanism diagram of the TE/C-RIE device in Figure 3b, the concentration of thermally excited electrons of n-type Bi₂Te₃ at the junction position increases rapidly, and the electrons spontaneously diffuse to the cold end under the action of the carrier concentration gradient, forming a thermoelectric current from the outside to the inside direction. A stable current output can be achieved when the number of thermally excited electrons is the same as the number of transferred

electrons. Similarly, p-type Bi_{0.5}Sb_{1.5}Te₃ generates a thermoelectric current from inside to the outside. Then the photothermal-induced electric signal can be realized by connecting the n-type and p-type thermoelectric legs in series as shown in Figure 3c.⁵⁰ For a specific thermoelectric material, the magnitude of this potential is directly determined by the temperature gradient induced by the photothermal effect. The TE, TE/C, and TE/C-RIE devices were subjected to light response tests under simulated natural light from a xenon lamp, as shown in Figure 3d. The TE device produced a stable response potential of 82.6 μV under 1 mW of simulated natural sunlight. Under the same illumination conditions, the TE/C and TE/C-RIE devices exhibited response potentials of 133.1 and 153.6 μV, respectively. It represents an enhancement of over 86% compared to that of the pure TE device. Moreover, all three devices exhibited rapid output and attenuation of electrical signals upon turning the light source on and off, demonstrating the effective detection capability of natural sunlight using the composite device. Figure S13 shows the light response time of TE, TE/C, and TE/C-RIE devices, which is

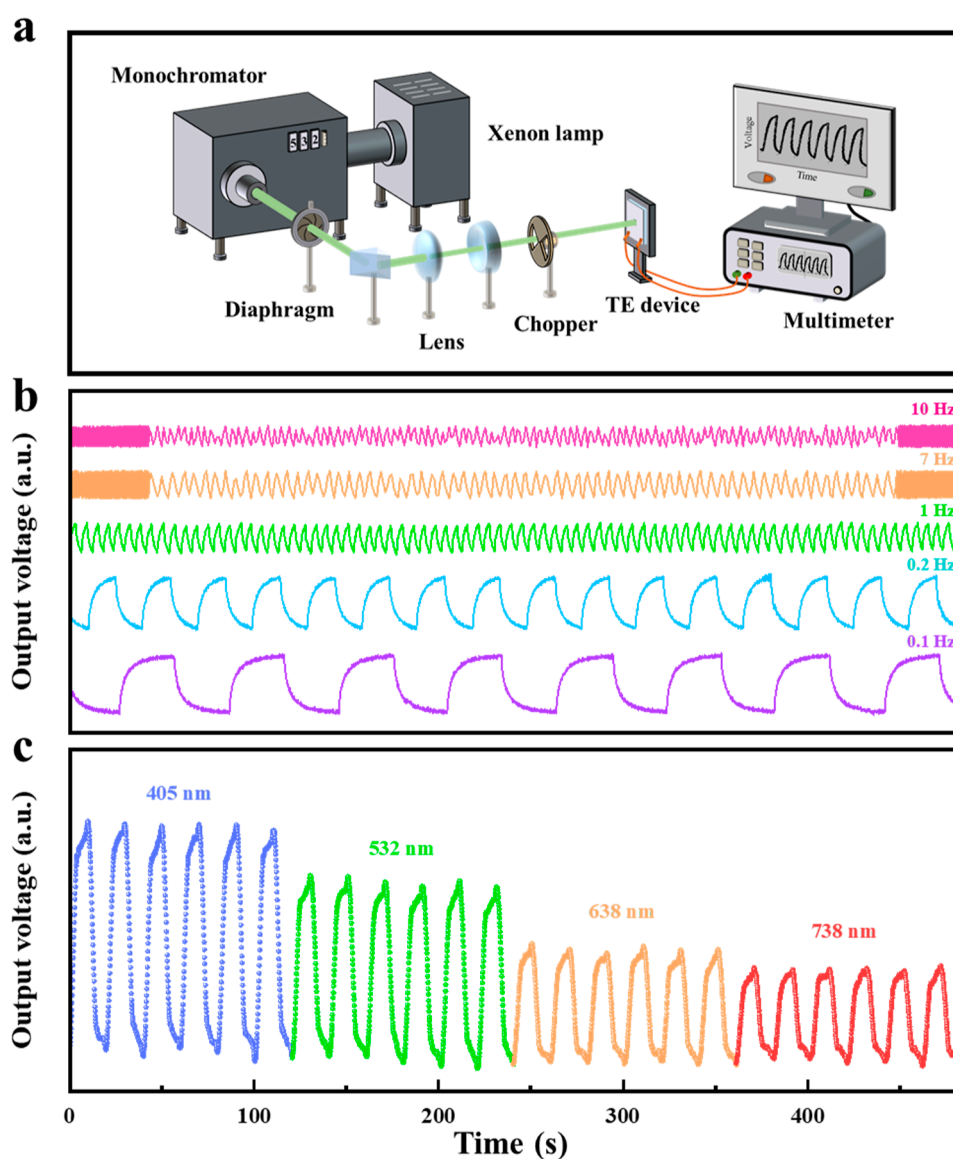


Figure 4. Light response performance of TE/C-RIE under different incident light conditions. (a) Schematic diagram of a light response test device. (b) Light response curves under different chopper frequencies (0.1, 0.2, 1, 7, and 10 Hz) of simulated natural light; the curves of 7 and 10 Hz are amplification curves in the time dimension. (c) Light response curves under different wavelength (405, 532, 638, and 738 nm) incident light irradiation.

generally defined as 10–90% signal change time.^{51,52} The rise/fall time of TE/C-RIE is 3.46/3.42 s; it is faster than TE/C and TE of 4.05/3.81 s and 4.94/5.35 s, which are close to the values reported for PTE detectors with similar size.^{32,52} The peak intensity of the differential curve of the light response test results shown in Figure 3e can also effectively reflect the response sensitivity of the device to light illumination. These results demonstrate that the addition of the light-absorbing C-RIE layer can effectively improve the light response sensitivity of the composite device. The calculated light responsivities for different devices are listed in Figure 3f. The TE device exhibits a natural light responsivity of 82.61 mV W⁻¹, while the TE/C-RIE device achieves an increased light responsivity of 153.58 mV W⁻¹. In addition, the specific detectivity parameter of the photodetector is commonly used to evaluate its ability to detect the weakest illuminations from noise. Due to the unique response mechanism of photodetectors based on the PTE effect, they can operate without requiring additional bias

conditions. Hence, the primary source of response noise for this type of device is Johnson–Nyquist noise.^{8,53,54} The specific detectivity of the TE/C-RIE device under 1 mW simulated natural light irradiation was calculated by the formula F4 shown in the Supporting Information. The result shown in Figure 3f reached 6.97×10^6 cm Hz^{1/2} W⁻¹, whereas the TE device has a specific detectivity of 3.75×10^6 cm Hz^{1/2} W⁻¹, resulting in an improvement rate of 85.91%. Furthermore, as indicated in Figure S14a, the equivalent noise power of the composite device gradually decreased with the modification of the light-absorbing C film. This enhancement originates from the significantly improved light absorption efficiency of the composite device due to the roughened C layer. Thus, modification of the C-RIE light-absorbing layer effectively enhances the light detection capability of the composite photodetector. The response ability of the TE/C-RIE device under different power simulated natural light illumination was characterized, and the results are presented in

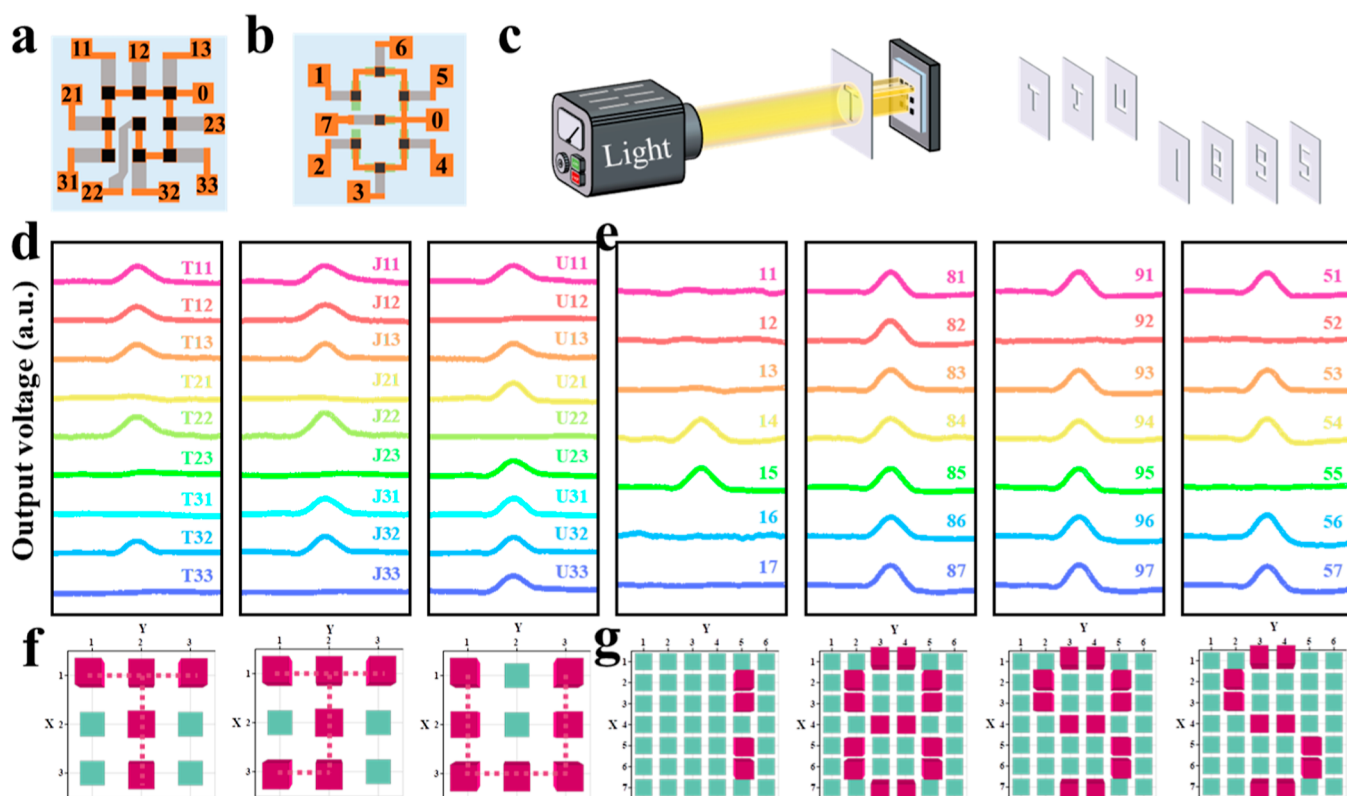


Figure 5. Light imaging performance of TE/C-RIE integrated devices. Schematic diagram of the electrode structure of the letter (a) and digit (b) integrated devices. (c) Schematic diagram of the light imaging test process. Output potential results of TE/C-RIE under the irradiation of letter-shaped (d) and digit-shaped (e) light sources. Output imaging patterns of letters (f) and digits (g).

Figure 3g. The device demonstrates stable light response signals under varying illumination powers. The corresponding light responsivities were 109.55, 153.58, 117.39, and 95.99 mV W^{-1} for simulated natural light powers of 0.5, 1, 1.9, and 3 mW, respectively. The light responsivity and specific detectivity, depicted in **Figure S14b**, initially increase and then decrease as the light source intensity rises. The decrease in the responsivity at high power levels can be attributed to diminishing temperature gradients across the thermoelectric units caused by thermal diffusion with an increase in light intensity. Conversely, the decrease in the responsivity at low power levels stems from the weakened photothermal efficiency of the device's photosensitive region under low-energy light inputs. Currently, in order to ensure the effective maintenance of the temperature gradient across the thermoelectric units, most researchers use a focused light source as the incident light for the performance evaluation of PTE photodetectors. However, this approach does not fully reflect the actual detection capabilities of PTE photodetectors. Therefore, the TE/C-RIE device was fully exposed to simulated solar light intensity for light response testing, as shown in the inserted image of **Figure 3h**. The device exhibits a response potential of 100 μV within 3 s and further reaches a stable output of 240 μV within 200 s. Meanwhile, the response potential of the device remains unchanged when fully exposed to simulated sunlight for 30 min. By encapsulation of the light-sensitive C layer of the composite device with PDMS, the photodetection performance of the TE/C-RIE device in water was investigated. The testing setup and results are shown in **Figure 3i**. It can be observed that the device still exhibits rapid light response capability under 1 time of simulated solar light

intensity. Which the maximum output potential can maintain over 95% of the value in air tests. The stability of the TE/C-RIE device under atmospheric conditions was also characterized. **Figure S15a** shows the light response performance comparison of the initial TE/C-RIE and the composite device stored in an air environment for 1 year. As can be seen, the device placed in an air environment for 1 year can still maintain more than 95% of the detection capability of the initial device. The surface morphology changes are shown in **Figure S15d,e**, with no significant difference from the initial device. Furthermore, XPS characterization of Bi_2Te_3 with weaker antioxidant capacity was performed, and the results are shown in **Figure S15f,g**. It can be seen that after being placed in an air environment, the intensity of the oxidation peak at the slightly higher binding energy position has increased, but the peak position has not changed significantly. Therefore, a little decrease in the light detection performance of the composite device can be attributed to the slight oxidation of the material, but it can still maintain more than 95% of the initial performance, proving that the device has excellent stability. These results validate the excellent potential of the TE/C-RIE composite photodetector for practical applications.

In order to explore the light detection potential of the TE/C-RIE composite photodetector in various scenarios, the device was tested under different chopping frequencies and monochromatic light irradiation. **Figure 4a** illustrates the schematic diagram of the experimental setup, where a xenon lamp served as the incident light source. Different chopping frequencies were achieved by adjusting the output power of the chopper's driving power supply. Monochromatic light was obtained by passing the xenon lamp light through a

monochromator. Additionally, a lens group consisting of concave and convex lenses (as shown in Figure S16) was added to the optical path. It can improve the problem of severe power density degradation of the incident light after multiple reflections in the monochromator. Moreover, this lens combination ensured that incident light was irradiated onto the surface of the device in the form of parallel light, which can also avoid inaccurate test results caused by the induction of plasma effects on the material surface when the incident light converges by a single convex lens. The spot size of the incident light is $1\text{ mm} \times 1\text{ mm}$, which completely covers the sensitive region of the device. Figure 4b shows the light response test results of the TE/C-RIE device under simulated natural light chopping irradiation at frequencies of 0.1, 0.2, 1, 7, and 10 Hz. The results for the 7 and 10 Hz tests are magnified on the timescale to accurately distinguish the detection performance of the composite device. It can be observed that the composite device can achieve accurate switch response and recognition under different frequencies of light irradiation and maintain a stable output voltage signal in long-period switch tests. The slight differences in the response signal of the 7 and 10 Hz test curves are due to the decrease in the photothermal conversion efficiency during the high-frequency chopping process. Figure 4c demonstrates the detection capability of the TE/C-RIE composite device for monochromatic light with wavelengths of 405, 532, 638, and 738 nm. It can be seen that the device can achieve a fast response potential output for monochromatic light of different wavelengths. This is due to the strong light absorption ability and wide spectral absorption range of the rough C-film. As shown in Figure S17, the light responsivity and specific detectivity of the composite device gradually decrease with the increase in the tested wavelength. It is mainly attributed to the lower energy of longer-wavelength light compared to that of shorter-wavelength light, which weakens the interaction with the photosensitive C layer and results in a smaller temperature gradient on both sides of the thermoelectric unit. The composite device exhibits the highest responsivity and specific detectivity when irradiated with 405 nm monochromatic light, reaching values of 8.18 mV W^{-1} and $3.70 \times 10^5\text{ cm Hz}^{1/2}\text{ W}^{-1}$, respectively. Therefore, it is demonstrated that the composite device possesses excellent detection and response capabilities for multifrequency chopped light and multiwavelength incident light.

Based on the high-efficiency light detection capability of TE/C-RIE devices, integrated photoimaging devices were fabricated by combining physical deposition techniques with microfabrication processes, as shown in Figure 5a,b, for the recognition of letter- and digit-shaped light sources, respectively. Bi_2Te_3 was used as the functional thermoelectric material to fabricate the device in a single-leg structure. By associating the output electrical signals of each responsive unit with their corresponding position information, patterned light source imaging detection can be achieved. As depicted in Figure 5c, a xenon lamp was used as the simulated natural light source in the experiment. Stainless steel masked with different hollow patterns were added between the light source and the tested device to create light with various patterned information. The response test results of the letter-integrated device under T, J, and U (Tianjin University) patterned light source illumination are shown in Figure 5d. For example, when illuminated by a T-shaped light source, rapid thermoelectric potential signals were generated in the T11, T12, T13, T22, and T32 electrodes, while other electrodes did not show

obvious electrical signal outputs. Similarly, when the device was illuminated by J and U-shaped light sources, all thermoelectric electrodes in the illuminated areas achieved stable response outputs. Likewise, the digit-integrated device was used for imaging tests with digit patterns of 0–9, as shown in Figures 5e and S18a. The electrodes in the integrated device were still capable of effectively identifying the illuminated and nonilluminated areas. By associating the response electrical signals of each electrode in the letter-integrated device with their position coordinates, the results are exported as shown in Figure 5f. It can be seen that the imaging results are consistent with the shape of the incident light source. The higher response potential in the 22-position electrode is attributed to its longer thermoelectric leg length, which results in a higher temperature gradient at both ends of the thermoelectric leg under the same light source illumination. At the same time, the weak electrical signal output in the nonilluminated unit is due to the thermal diffusion between adjacent pixels. By assigning the response values of each photosensitive unit in the digit-integrated device to two parallel pixels and plotting them in a 6×7 matrix imaging diagram as shown in Figure S19. Figures 5g and S18b show that the integrated device can accurately recognize the digit-shaped light sources. Furthermore, the high consistency in thermoelectric unit size and the uniform distribution of pixel positions in this device lead to higher stability and uniformity in the output potential signals of the electrodes. Table S2 provides a comparison of the light response test results of similar PTE devices. It shows that the TE/C-RIE device fabricated in this work has a response performance comparable to that of chemically or gas-phase fabricated light detectors. Moreover, compared to the fabrication processes of other integrated imaging devices, the fabrication steps of the TE/C-RIE integrated device are simpler and more cost-effective. These results demonstrate the excellent performance of the TE/C-RIE device in the field of photodetection. Furthermore, the patterned integrated device fabricated using microfabrication technology enables accurate recognition of letter- and digit-shaped light sources. This provides potential guidance for the application of such devices in the wide-spectrum detection and complex optical imaging fields.

4. CONCLUSIONS

In this work, a composite TE/C-RIE photodetector based on the photothermal and thermoelectric effects is designed. In the experiment, PLD technology was used to successfully prepare functional BiTe -based thermoelectric films with high Seebeck coefficient (Bi_2Te_3 : $-188.6\text{ }\mu\text{V K}^{-1}$ and $\text{Bi}_{0.5}\text{Sb}_{1.5}\text{Te}_3$: $500.6\text{ }\mu\text{V K}^{-1}$). By utilizing the high light absorption ability of the C-RIE layer, the light absorption efficiency of the composite device can be increased to more than 95% in the range of 400–900 nm. Based on this, the TE/C-RIE composite device exhibits 85.91% higher light detection performance than the TE device. Benefiting from the excellent photosensitivity of the TE/C-RIE structure and the integration advantage of PLD technology, the composite structure was expanded to integrated photoimaging devices. It successfully realized the accurate identification of pattern-shaped light sources with letters (T, J, and U) and digits (0–9) by associating the electrical signals of each electrode with their corresponding position coordinates. This work provides good guidance for the design and preparation of high-performance PTE photodetectors and photoimaging devices. In addition, it also lays a foundation for the

development of PTE devices in the field of wide-spectrum detection and optical communication.

■ ASSOCIATED CONTENT

SI Supporting Information

The Supporting Information is available free of charge at <https://pubs.acs.org/doi/10.1021/acsami.4c07979>.

Simulation results and details; calculation formulas of R_v , NEP, and D ; preparation process diagram; EDS, XPS, XRD, conductivity, and Seebeck coefficients of Bi_2Te_3 and $\text{Bi}_{0.5}\text{Sb}_{1.5}\text{Te}_3$; SEM images and light absorption spectrum of C-RIE; response time of composite devices; stability characterization of composite device; light imaging results; surface roughness of C-RIE; device performance comparison; and schematic diagram of a photoimaging device (PDF)

■ AUTHOR INFORMATION

Corresponding Authors

Yanqing Ma – Tianjin International Center for Nanoparticles and Nanosystems and School of Precision Instrument and Optoelectronics Engineering, Tianjin University, Tianjin 300072, P. R. China; Tianjin Key Laboratory of Low-Dimensional Electronic Materials and Advanced Instrumentation, Tianjin 300072, PR China; orcid.org/0000-0002-3317-8273; Email: mayanqing@tju.edu.cn

Lei Ma – Tianjin International Center for Nanoparticles and Nanosystems, Tianjin University, Tianjin 300072, P. R. China; Tianjin Key Laboratory of Low-Dimensional Electronic Materials and Advanced Instrumentation, Tianjin 300072, PR China; orcid.org/0000-0002-2446-4833; Email: lei.ma@tju.edu.cn

Authors

Rongke Sun – Tianjin International Center for Nanoparticles and Nanosystems, Tianjin University, Tianjin 300072, P. R. China

Runan Guo – Tianjin International Center for Nanoparticles and Nanosystems, Tianjin University, Tianjin 300072, P. R. China

Xue Yu – Tianjin International Center for Nanoparticles and Nanosystems, Tianjin University, Tianjin 300072, P. R. China

Yanmei Ren – Tianjin International Center for Nanoparticles and Nanosystems, Tianjin University, Tianjin 300072, P. R. China

Ruoxi Wang – Tianjin International Center for Nanoparticles and Nanosystems, Tianjin University, Tianjin 300072, P. R. China

Pinggen Zou – Tianjin International Center for Nanoparticles and Nanosystems, Tianjin University, Tianjin 300072, P. R. China

Zhi Chen – Tianjin International Center for Nanoparticles and Nanosystems, Tianjin University, Tianjin 300072, P. R. China

Rui Xu – Tianjin International Center for Nanoparticles and Nanosystems, Tianjin University, Tianjin 300072, P. R. China

Complete contact information is available at: <https://pubs.acs.org/doi/10.1021/acsami.4c07979>

Author Contributions

R.S.: Methodology, investigation, data curation, and writing—original draft preparation. R.G., X.Y., Y.R., and R.W.: Investigation and data curation. P.Z.: Simulation. Z.C.: Software circuit. R.X.: Writing—review and editing. Y.M.: Writing—review and editing, and supervision. L.M.: Conceptualization, supervision, methodology, validation, and writing—review and editing.

Notes

The authors declare no competing financial interest.

■ ACKNOWLEDGMENTS

This work was financially supported by the National Key R&D Program of China (no. 2022YFC3006303).

■ REFERENCES

- (1) He, X.; Fujimura, N.; Lloyd, J. M.; Erickson, K. J.; Talin, A. A.; Zhang, Q.; Gao, W.; Jiang, Q.; Kawano, Y.; Hauge, R. H.; et al. Carbon nanotube terahertz detector. *Nano Lett.* **2014**, *14* (7), 3953–3958.
- (2) Bao, C.; Yang, J.; Bai, S.; Xu, W.; Yan, Z.; Xu, Q.; Liu, J.; Zhang, W.; Gao, F. High performance and stable all-inorganic metal halide perovskite-based photodetectors for optical communication applications. *Adv. Mater.* **2018**, *30* (38), 1803422.
- (3) Hainey, M. F., Jr.; Mano, T.; Kasaya, T.; Ochiai, T.; Osato, H.; Watanabe, K.; Sugimoto, Y.; Kawazu, T.; Arai, Y.; Shigetou, A. Near-field resonant photon sorting applied: dual-band metasurface quantum well infrared photodetectors for gas sensing. *Nanophotonics* **2020**, *9* (16), 4775–4784.
- (4) Li, L.; Chen, H.; Fang, Z.; Meng, X.; Zuo, C.; Lv, M.; Tian, Y.; Fang, Y.; Xiao, Z.; Shan, C.; et al. An electrically modulated single-color/dual-color imaging photodetector. *Adv. Mater.* **2020**, *32* (24), 1907257.
- (5) Guo, B.; Wang, Y.; Peng, C.; Zhang, H.; Luo, G.; Le, H.; Gmachl, C.; Sivco, D.; Peabody, M.; Cho, A. Y. Laser-based mid-infrared reflectance imaging of biological tissues. *Opt. Express* **2004**, *12* (1), 208–219.
- (6) Hsu, A. L.; Herring, P. K.; Gabor, N. M.; Ha, S.; Shin, Y. C.; Song, Y.; Chin, M.; Dubey, M.; Chandrakasan, A. P.; Kong, J.; et al. Graphene-based thermopile for thermal imaging applications. *Nano Lett.* **2015**, *15* (11), 7211–7216.
- (7) Lu, X.; Sun, L.; Jiang, P.; Bao, X. Progress of photodetectors based on the photothermoelectric effect. *Adv. Mater.* **2019**, *31* (50), 1902044.
- (8) Wang, R.; He, Z.; Wang, J.-L.; Liu, J.-Y.; Liu, J.-W.; Yu, S.-H. Manipulating nanowire structures for an enhanced broad-band flexible photothermoelectric photodetector. *Nano Lett.* **2022**, *22* (14), 5929–5935.
- (9) Lai, Y. S.; Tsai, C. Y.; Chang, C. K.; Huang, C. Y.; Hsiao, V. K.; Su, Y. O. Photothermoelectric effects in nanoporous silicon. *Adv. Mater.* **2016**, *28* (13), 2644–2648.
- (10) Zhao, T.; Yang, L.-Z.; Zhou, Y.; Liao, H.-J.; Huang, Z.-Y.; Li, J.; Lu, X.; Zhou, X.-Y. Thermoelectric performance of $(\text{AgBiTe}_2)_{1-x}(\text{SnTe})_x$ with stable cubic enabled by enhanced configurational entropy. *Rare Met.* **2022**, *41* (12), 4149–4155.
- (11) Chen, Z.; Zhang, X.; Lin, S.; Chen, L.; Pei, Y. Rationalizing phonon dispersion for lattice thermal conductivity of solids. *Natl. Sci. Rev.* **2018**, *5* (6), 888–894.
- (12) Chen, T.; Fan, P.; Zheng, Z.; Zhang, D.; Cai, X.; Liang, G.; Cai, Z. Influence of substrate temperature on structural and thermoelectric properties of antimony telluride thin films fabricated by RF and DC cosputtering. *J. Electron. Mater.* **2012**, *41*, 679–683.
- (13) Qi, Y.; Wang, Z.; Zhang, M.; Yang, F.; Wang, X. Thermoelectric devices based on one-dimensional nanostructures. *J. Mater. Chem. A* **2013**, *1* (20), 6110–6124.
- (14) Liu, Y.; Lan, X.; Xu, J.; Zhou, W.; Liu, C.; Liu, C.; Liu, P.; Li, M.; Jiang, F. Organic/inorganic hybrid boosting energy harvesting

- based on the photothermoelectric effect. *ACS Appl. Mater. Interfaces* **2021**, *13* (36), 43155–43162.
- (15) He, M.; Lin, Y.-J.; Chiu, C.-M.; Yang, W.; Zhang, B.; Yun, D.; Xie, Y.; Lin, Z.-H. A flexible photo-thermoelectric nanogenerator based on MoS₂/PU photothermal layer for infrared light harvesting. *Nano Energy* **2018**, *49*, 588–595.
- (16) Ouyang, B.; Chang, C.; Zhao, L.-D.; Wang, Z. L.; Yang, Y. Thermo-photoelectric coupled effect induced electricity in N-type SnSe:Br single crystals for enhanced self-powered photodetectors. *Nano Energy* **2019**, *66*, 104111.
- (17) Gu, Y.; Yao, X.; Geng, H.; Long, M.; Guan, G.; Hu, M.; Han, M. Large-area, flexible, and dual-source co-evaporated Cs₃Cu₂I₅ nanolayer to construct ultra-broadband photothermoelectric detector from visible to terahertz. *ACS Appl. Electron. Mater.* **2022**, *4* (2), 663–671.
- (18) Yao, J.; Zheng, Z.; Yang, G. All-layered 2D optoelectronics: a high-performance UV–vis–NIR broadband SnSe photodetector with Bi₂Te₃ topological insulator electrodes. *Adv. Funct. Mater.* **2017**, *27* (33), 1701823.
- (19) Guo, Z.; Zhu, W.; Yu, Y.; Deng, Y. Photo-thermoelectric thin-film generator and sensor with ultrahigh output voltage and large responsivity. *IEEE Electron Device Lett.* **2019**, *40* (11), 1832–1835.
- (20) Bailini, A.; Donati, F.; Zamboni, M.; Russo, V.; Passoni, M.; Casari, C. S.; Li Bassi, A.; Bottani, C. E. Pulsed laser deposition of Bi₂Te₃ thermoelectric films. *Appl. Surf. Sci.* **2007**, *254* (4), 1249–1254.
- (21) Zhang, H.; Momand, J.; Levinsky, J.; Guo, Q.; Zhu, X.; ten Brink, G. H.; Blake, G. R.; Palasantzas, G.; Kooi, B. J. Nanostructure and thermal power of highly-textured and single-crystal-like Bi₂Te₃ thin films. *Nano Res.* **2022**, *15* (3), 2382–2390.
- (22) Shi, X.-L.; Zou, J.; Chen, Z.-G. Advanced thermoelectric design: from materials and structures to devices. *Chem. Rev.* **2020**, *120* (15), 7399–7515.
- (23) Mamur, H.; Bhuiyan, M.; Korkmaz, F.; Nil, M. A review on bismuth telluride (Bi₂Te₃) nanostructure for thermoelectric applications. *Renew. Sustain. Energy Rev.* **2018**, *82*, 4159–4169.
- (24) Pei, J.; Cai, B.; Zhuang, H.-L.; Li, J.-F. Bi₂Te₃-based applied thermoelectric materials: research advances and new challenges. *Natl. Sci. Rev.* **2020**, *7* (12), 1856–1858.
- (25) Hong, M.; Chen, Z.-G.; Zou, J. Fundamental and progress of Bi₂Te₃-based thermoelectric materials. *Chin. Phys. B* **2018**, *27* (4), 048403.
- (26) Hu, L.; Meng, F.; Zhou, Y.; Li, J.; Benton, A.; Li, J.; Liu, F.; Zhang, C.; Xie, H.; He, J. Leveraging deep levels in narrow bandgap Bi_{0.5}Sb_{1.5}Te₃ for record-high zT_{ave} near room temperature. *Adv. Funct. Mater.* **2020**, *30* (45), 2005202.
- (27) Liu, W.; Wang, W.; Guan, Z.; Xu, H. A plasmon modulated photothermoelectric photodetector in silicon nanostripes. *Nanoscale* **2019**, *11* (11), 4918–4924.
- (28) Shautsova, V.; Sidiropoulos, T.; Xiao, X.; Gusken, N. A.; Black, N. C.; Gilbertson, A. M.; Giannini, V.; Maier, S. A.; Cohen, L. F.; Oulton, R. F. Plasmon induced thermoelectric effect in graphene. *Nat. Commun.* **2018**, *9* (1), 5190.
- (29) Li, X.; Sheng, M.; Liang, J.; Zheng, J.; Zheng, Y.; Wang, S.; Li, Q.; Zhao, L. D.; Deng, Y.; Wang, Y. Significantly boosted photothermoelectric effect via carrier injection in Au decorated SWCNT films for infrared detection. *Adv. Funct. Mater.* **2023**, *33*, 2303352.
- (30) Webb, J. A.; Bardhan, R. Emerging advances in nanomedicine with engineered gold nanostructures. *Nanoscale* **2014**, *6* (5), 2502–2530.
- (31) Wu, D.; Yan, K.; Zhou, Y.; Wang, H.; Lin, L.; Peng, H.; Liu, Z. Plasmon-enhanced photothermoelectric conversion in chemical vapor deposited graphene p–n junctions. *J. Am. Chem. Soc.* **2013**, *135* (30), 10926–10929.
- (32) Yang, Z.-y.; Jin, X.-z.; Huang, C.-h.; Lei, Y.-z.; Wang, Y. Constructing A/B-side heterogeneous asynchronous structure with Ag₂Se layers and bushy-like PPy toward high-performance flexible photo-thermoelectric generators. *ACS Appl. Mater. Interfaces* **2022**, *14* (29), 33370–33382.
- (33) Makala, R. S.; Jagannadham, K.; Sales, B. C. Pulsed laser deposition of Bi₂Te₃-based thermoelectric thin films. *J. Appl. Phys.* **2003**, *94* (6), 3907–3918.
- (34) Yu, Z.; Wang, X.; Du, Y.; Aminorroaya-Yamni, S.; Zhang, C.; Chuang, K.; Li, S. Fabrication and characterization of textured Bi₂Te₃ thermoelectric thin films prepared on glass substrates at room temperature using pulsed laser deposition. *J. Cryst. Growth* **2013**, *362*, 247–251.
- (35) Zhao, C.; Wang, D.; Cao, J.; Zeng, Z.; Zhang, B.; Pan, J.; Liu, D.; Liu, S.; Jiao, S.; Chen, T.; Liu, G.; Fang, X.; Zhao, L.; Wang, J. Highly efficient 1D p-Te/2D n-Bi₂Te₃ heterojunction self-driven broadband photodetector. *Nano Research* **2024**, *17*, 1864–1874.
- (36) Shallenberger, J. R.; Smyth, C. M.; Addou, R.; Wallace, R. M. 2D bismuth telluride analyzed by XPS. *Surf. Sci. Spectra* **2019**, *26* (2), 024011.
- (37) Zhao, Y.; Burda, C. Chemical synthesis of Bi_{0.5}Sb_{1.5}Te₃ nanocrystals and their surface oxidation properties. *ACS Appl. Mater. Interfaces* **2009**, *1* (6), 1259–1263.
- (38) Lwin, M. L.; Dharmiah, P.; Yoon, S.-M.; Song, S. H.; Kim, H. S.; Lee, J.-H.; Ghomashchi, R.; Hong, S.-J. Correlation with the composition of the different parts of p-type Bi_{0.5}Sb_{1.5}Te₃ sintered bulks and their thermoelectric characteristics. *J. Alloys Compd.* **2020**, *845*, 156114.
- (39) Ji, X.; Tang, Z.; Liu, H.; Kang, Y.; Chen, L.; Dong, J.; Chen, W.; Kong, N.; Tao, W.; Xie, T. Thermoelectric effect mediated cancer thermoelectric therapy and surgical adjuvant treatment. *Adv. Mater.* **2022**, *35*, 2207391.
- (40) Tritt, T. M. Thermoelectric materials: principles, structure, properties, and applications. In *Encyclopedia of Materials: Science and Technology*; Elsevier, 2002.
- (41) Zhang, S.-S.; Yang, D.-F.; Shaheen, N.; Shen, X.-C.; Xie, D.-D.; Yan, Y.-C.; Lu, X.; Zhou, X.-Y. Enhanced thermoelectric performance of CoSbS_{0.85}Se_{0.15} by point defect. *Rare Met.* **2018**, *37*, 326–332.
- (42) Hong, M.; Chen, Z.-G.; Yang, L.; Liao, Z.-M.; Zou, Y.-C.; Chen, Y.-H.; Matsumura, S.; Zou, J. Achieving $zT > 2$ in p-type AgSbTe_{2-x}Se_x alloys via exploring the extra light valence band and introducing dense stacking faults. *Adv. Energy Mater.* **2018**, *8* (9), 1702333.
- (43) Wei, J.; Yang, L.; Ma, Z.; Song, P.; Zhang, M.; Ma, J.; Yang, F.; Wang, X. Review of current high-ZT thermoelectric materials. *J. Mater. Sci.* **2020**, *55*, 12642–12704.
- (44) Cao, T.; Shi, X.-L.; Li, M.; Hu, B.; Chen, W.; Liu, W.-D.; Lyu, W.; MacLeod, J.; Chen, Z.-G. Advances in bismuth-telluride-based thermoelectric devices: progress and challenges. *eScience* **2023**, *3*, 100122.
- (45) Xu, D.; Li, Z.; Li, L.; Wang, J. Insights into the photothermal conversion of 2D MXene nanomaterials: synthesis, mechanism, and applications. *Adv. Funct. Mater.* **2020**, *30* (47), 2000712.
- (46) Cheng, P.; Doll, J.; Romanus, H.; Wang, H.; van Aken, P. A.; Wang, D.; Schaaf, P. Reactive magnetron sputtering of large-scale 3D aluminum-based plasmonic nanostructure for both light-induced thermal imaging and photo-thermoelectric conversion. *Adv. Opt. Mater.* **2023**, *11* (6), 2202664.
- (47) Bao, J.; Chen, W.; Liu, T.; Zhu, Y.; Jin, P.; Wang, L.; Liu, J.; Wei, Y.; Li, Y. Bifunctional Au-Fe₃O₄ nanoparticles for protein separation. *ACS Nano* **2007**, *1* (4), 293–298.
- (48) He, W.; Zhou, L.; Wang, M.; Cao, Y.; Chen, X.; Hou, X. Structure development of carbon-based solar-driven water evaporation systems. *Sci. Bull.* **2021**, *66* (14), 1472–1483.
- (49) Li, M.; Shi, M.; Wang, B.; Zhang, C.; Yang, S.; Yang, Y.; Zhou, N.; Guo, X.; Chen, D.; Li, S.; et al. Quasi-ordered nanoforests with hybrid plasmon resonances for broadband absorption and photo-detection. *Adv. Funct. Mater.* **2021**, *31* (38), 2102840.
- (50) Ren, Y.; Sun, R.; Yu, X.; Wang, R.; Zhang, W.; Zhu, X.; Ma, Y.; Ma, L. A systematic study on synthesis parameters and thermoelectric properties of tellurium nanowire bundles. *Mater. Adv.* **2023**, *4* (19), 4455–4462.

(51) Lu, X.; Jiang, P.; Bao, X. Phonon-enhanced photothermoelectric effect in SrTiO₃ ultra-broadband photodetector. *Nat. Commun.* **2019**, *10* (1), 138.

(52) Liu, Y.; Hu, Q.; Cao, Y.; Wang, P.; Wei, J.; Wu, W.; Wang, J.; Huang, F.; Sun, J.-L. High-performance ultrabroadband photodetector based on photothermoelectric effect. *ACS Appl. Mater. Interfaces* **2022**, *14* (25), 29077–29086.

(53) Mauser, K. W.; Kim, S.; Mitrovic, S.; Fleischman, D.; Pala, R.; Schwab, K.; Atwater, H. A. Resonant thermoelectric nanophotonics. *Nat. Nanotechnol.* **2017**, *12* (8), 770–775.

(54) Zhang, J.; Bang, J. H.; Tang, C.; Kamat, P. V. Tailored TiO₂-SrTiO₃ heterostructure nanotube arrays for improved photoelectrochemical performance. *ACS Nano* **2010**, *4* (1), 387–395.